Neuron
Article

Two Distinct Channels of Olfactory Bulb Output

Izumi Fukunaga,[1] Manuel Berning,[1] Mihaly Kollo,[1] Anja Schmaltz,[1] and Andreas T. Schaefer[1,2,*]
[1]Behavioural Neurophysiology, Max-Planck-Institute for Medical Research, Jahnstr. 29, 69120 Heidelberg, Germany
[2]Institute of Anatomy and Cell Biology, University of Heidelberg, INF 307, 69120 Heidelberg, Germany
*Correspondence: schaefer@mpimf-heidelberg.mpg.de
http://dx.doi.org/10.1016/j.neuron.2012.05.017

SUMMARY

Rhythmic neural activity is a hallmark of brain function, used ubiquitously to structure neural information. In mammalian olfaction, repetitive sniffing sets the principal rhythm but little is known about its role in sensory coding. Here, we show that mitral and tufted cells, the two main classes of olfactory bulb projection neurons, tightly lock to this rhythm, but to opposing phases of the sniff cycle. This phase shift is established by local inhibition that selectively delays mitral cell activity. Furthermore, while tufted cell phase is unperturbed in response to purely excitatory odorants, mitral cell phase is advanced in a graded, stimulus-dependent manner. Thus, phase separation by inhibition forms the basis for two distinct channels of olfactory processing.

INTRODUCTION

Rhythms and time references are commonly used in signal processing to coordinate and reliably encode information. Similarly, many biological systems structure the environmental representation into cycles of activity: the rodent somatosensory system makes use of whisking, repeated at ~5–15 Hz to sample the tactile environment (Diamond et al., 2008; Welker, 1964); in vision, primates parse the scenery with patterns of eye movements and fixations at ~3 Hz (Bosman et al., 2009; Schroeder et al., 2010); more centrally, in the hippocampus, spatial information is encoded relative to a prominent theta rhythm (O'Keefe and Recce, 1993). In mammalian olfaction, the chemical environment is explored with 2–12 Hz repetitive sniffing (Welker, 1964). As a consequence, electrical activity in different brain areas is synchronized to these rhythms (Macrides and Chorover, 1972; O'Keefe and Recce, 1993; Schroeder et al., 2010). Timing relative to the sniff rhythm in turn can serve as a base for efficient odor discrimination (Smear et al., 2011).

In the olfactory bulb (OB), the first processing stage of the mammalian olfactory system, sniff-coupled inputs from olfactory sensory neurons (OSN) are transmitted to principal neurons (Cang and Isaacson, 2003; Margrie and Schaefer, 2003, Phillips et al., 2012), that in turn project to olfactory cortical areas, such as amygdala, piriform or entorhinal cortical areas (Ghosh et al., 2011; Haberly and Price, 1977; Miyamichi et al., 2011; Nagayama et al., 2010; Sosulski et al., 2011). These principal neurons segregate into at least two classes, mitral cells (MCs) and tufted cells (TCs), distinguished by their dendritic morphology and soma locations (Haberly and Price, 1977; Mori et al., 1983; Orona et al., 1984). Axonal projections of TCs are restricted to the anterior part of the piriform cortex and more rostral structures, while MCs cover, among others, the entire piriform cortex (Haberly and Price, 1977; Nagayama et al., 2010). Thus, spatially, information is relayed to overlapping parts of olfactory cortex by the two types of principal neurons of the OB. Whether these two streams also encode olfactory information differently, e.g., with different temporal dynamics, has remained unclear (Buonviso et al., 2003; Nagayama et al., 2004).

RESULTS

Respiration-Locking of Olfactory Bulb Principal Neurons

We performed whole-cell recordings in vivo from principal neurons of the mouse OB (Figure 1A). The majority of cells (69/83) showed significant subthreshold membrane potential oscillations tightly coupled to the sniff rhythm (Figure 1B; Figures S6 and S7 available online). For each individual cell this coupling was reliable and the preferred phase remained stable over time (Figure S8). Surprisingly, however, across the population of cells the preferred phase was widely distributed across the sniff cycle (Figures 1B and 1C), as was the preferred phase of action potential (AP) firing (Figure 1D). The preferred phase of principal neurons in awake, head-fixed mice showed similar diversity (Figure S1).

MCs and TCs Lock to Distinct Phases of the Sniff Cycle

To assess the basis of such heterogeneity, in a subset of recordings, we filled cells with biocytin during the recording, allowing post hoc morphological reconstruction and neuronal identification (Figures 2A–2D, n = 15, for a complete gallery see Figure S2). Morphological analysis of these principal neurons based on four basic and robust parameters (soma position, dendritic position in the EPL, soma size, dendritic length) showed two clusters (Figures 2E–2J), corresponding to the classical definition of MCs and TCs (Macrides and Schneider, 1982; Mori et al., 1983).

This morphological identification allowed us to unambiguously correlate the electrophysiologically measured sniff phase preference with the cell type. Indeed, the preferred phase of MC depolarization was tightly clustered during the inhalation period, whereas that of TCs matched the exhalation phase (Figures 2C, 2D, 2K, 3, and S2). As a consequence, the preferred phase of AP discharge was also distinct for MCs and TCs (Figures 3A–3C and 3F).

The two morphologically defined cell classes preferred perfectly non-overlapping phases of the sniff cycle (Figures 3E

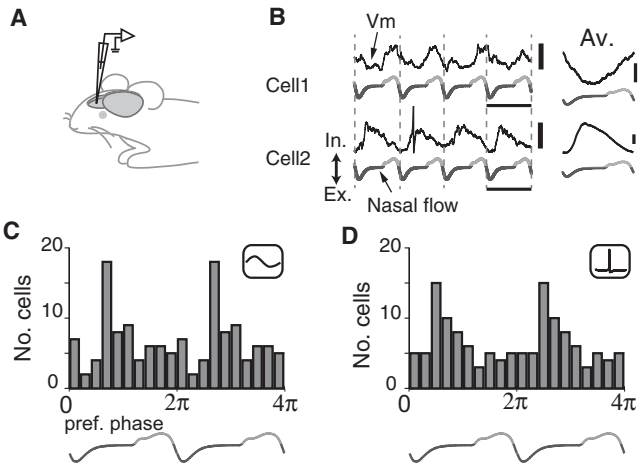

Figure 1. Olfactory Bulb Principal Neurons Lock to Heterogeneous Phases of the Sniff Cycle

(A) Experimental configuration. Whole cell patch clamp recordings were made from principal neurons in the olfactory bulb of anaesthetized mice.

(B) Examples of membrane potential oscillation (black) from two different cells with respect to the sniff cycle (gray; nasal air flow). The first cell shows oscillation peaks during the inhalation period (light gray), while the second cell shows peaks during the exhalation period (dark gray). Scale bars represent 10mV (raw trace) and 1mV (average over all sniff cycles), sniff cycle length = 402 and 330 ms. Action potentials (APs) clipped for display purposes.

(C) Distribution of preferred sniff phases from all principal cells recorded that were significantly coupled to sniffing (n = 69/83 cells; Figures S6 and S7).

(D) Preferred average phase of spontaneous action potentials (n = 69 cells). Data is repeated over two sniff cycles to visualize the cyclical nature.

See also Figure S1.

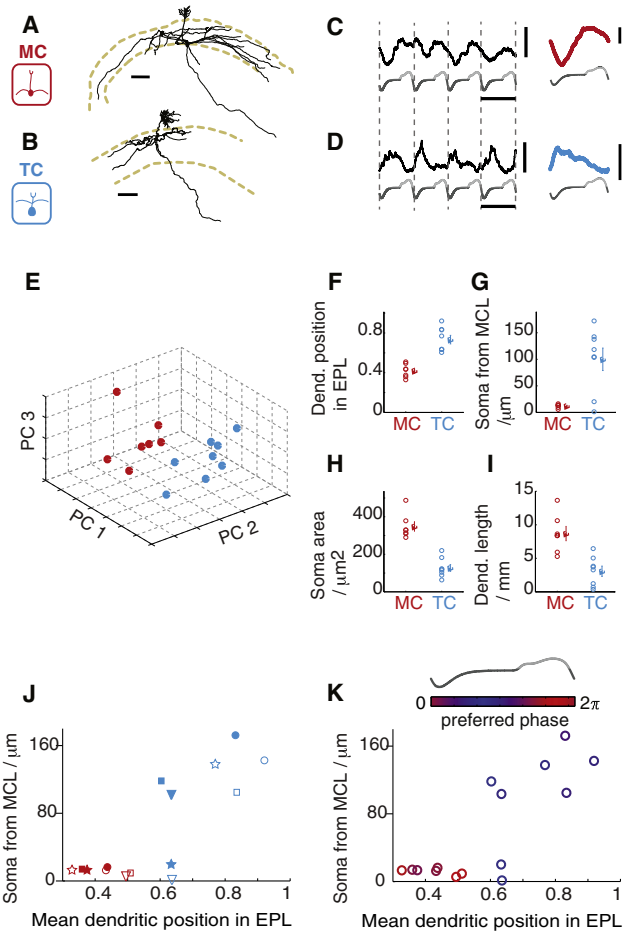

Figure 2. Distinct Sniff Coupling Corresponds to Morphologically Distinct Mitral and Tufted Cells

(A–D) Examples of reconstructed and morphologically identified mitral cells (MCs) (A) and tufted cells (TCs) (B) (scale bar represents 100 µm) and their sniff-coupled membrane potential oscillation (C and D). Scale bars represent 10mV (raw trace), 2mV (average), sniff cycle length = 390 and 360 ms.

(E) Reconstructed neurons were classified into two classes (red and blue, respectively) by EM clustering based on morphological parameters shown in (F–I).

(F) Dendritic position in EPL, weighted by volume; 0.42 ± 0.03 MCs, 0.73 ± 0.04 TCs; (G) soma distance from MCL; 12.07 ± 1.33 µm MCs, 100.03 ± 21.09 µm TCs; (H) soma area; 348.28 ± 25.36 μm^2 MCs, 127.09 ± 17.93 μm^2 TCs; (I) total dendritic lengths; 8.69 ± 1.07 mm MCs, 3.07 ± 0.76 mm TCs Values are mean and SEM.

(J) Plotting the 15 morphologically reconstructed neurons as a function of those parameters classically used to distinguish MCs and TCs, namely soma position and dendritic ramification showed that the red cluster indeed corresponds to MCs, whereas the blue cluster denotes TCs. For individual morphologies see Figure S2. For TCs 14 and 15, soma positions could be identified unambiguously but dendritic arborization was only estimated from partial staining and reconstruction.

(K) Phase preference is indicated in color code for the same cells. Note the tight correspondence between the subthreshold membrane oscillation phase and the morphology, namely, the soma locations and the positions of the lateral dendrites in the external plexiform layer (EPL). Within the TC population, no further heterogeneity was found, i.e., superficial, middle, and deep TCs could not be distinguished based on the preferred phase.

See also Figure S8.

and 3F). MCs and TCs can therefore be reliably distinguished based on their preferred phase of membrane potential or action potential firing, allowing the unambiguous identification of MC and TC solely by phase (labeled "phase MCs" [MC_Ps], and "phase TCs" [TC_Ps]). Other physiological measures in turn did not show any distinctive difference between the two groups (Figure S3).

Inhibition Underlies the Phase Shift between MCs and TCs

MCs and TCs are excited primarily within a glomerulus, where olfactory sensory neuron (OSN) axons form glutamatergic synapses onto projection neurons. These inputs are strongly sniff-modulated but the time course of inputs within a glomerulus is thought to be homogeneous (Wachowiak et al., 2004). Thus, the phase difference between MCs and TCs is likely to be generated by either OB circuitry or differential inputs from other brain areas. To assess the potential role of inhibitory interneurons, we performed whole-cell recordings while pharmacologically blocking fast GABAergic transmission (Figure 4A). In order to avoid the epileptic discharges that are common with applications of GABAergic antagonists alone in vivo (Figures S4A–S4D), we applied a titrated mixture of a $GABA_A$ antagonist, gabazine (0.4 mM), and a potent $GABA_A$ agonist, muscimol (2 mM). The high effective dose of exogenous drugs should outcompete endogenous GABA for action on $GABA_A$ receptors (Bao et al.,

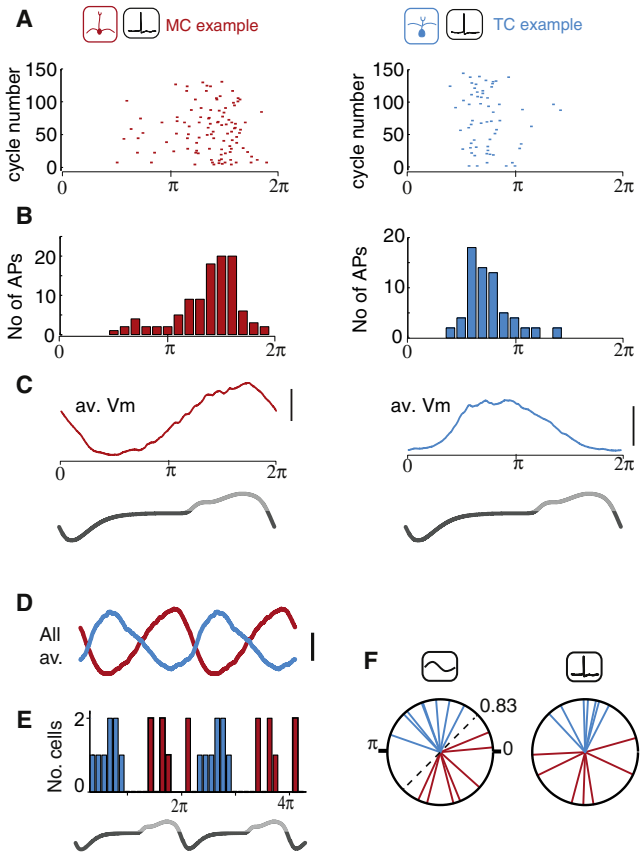

Figure 3. MCs and TCs Subthreshold Oscillation and AP Discharge Lock to Nonoverlapping Phases of the Sniff Cycle

(A–C) Examples from an MC (left, red) and a TC (right, blue) show that action potentials, shown as raster plots (A) and histograms (B) occur during the rising and peak phase of the sniff-coupled membrane oscillations (C) and at distinct sniff phases.

(D) Sniff-aligned averages of subthreshold membrane potential for all morphologically identified mitral (red; n = 7 cells) and tufted (blue; n = 8 cells) cells. Scale bar represents 1mV.

(E) Histogram of preferred subthreshold phase for morphologically identified MCs (red) and TCs (blue).

(F) Phase diagram of peak subthreshold oscillation phase (left) and peak action potential phase (right) of morphologically identified MCs (red) and TCs (blue). Dotted line indicates a separation between MCs and TCs based on preferred subthreshold phase. The preferred subthreshold phase for MCs ranged 4.32–0.41 Rad (5.31 ± 0.88 Rad, mean ± SD) and for TC ranged 1.09–2.81 Rad (1.94 ± 0.51 Rad, mean ± SD). For APs, the preferred average phase for MCs ranged 3.19–0.27 Rad (4.67 ± 1.15 Rad, mean ± SD) and for TC ranged 1.10–2.33 Rad (1.60 ± 0.40 Rad, mean ± SD).

See also Figure S3.

2002), consequently clamping $GABA_A$-mediated inhibition without substantially altering network excitability. This requires that the blockade of $GABA_A$ receptors by gabazine is on average closely counterbalanced by muscimol-mediated, stimulus-independent opening of synaptic and extrasynaptic $GABA_A$ receptors. Consistent with this, the "$GABA_A$-clamp" resulted in comparable average baseline firing rates as well as input resistance, and subthreshold oscillatory activity was efficiently maintained (Figures 4B–4D). Notably, synaptic inhibition, as measured by evoking recurrent inhibition in vivo (Abraham et al., 2010), was indeed robustly and significantly reduced (1,186mV ± 82mV × ms control versus 741mV ± 109mV × ms, p = 0.004, 11 cells; Figure 4E). Thus, $GABA_A$-clamp through combined application of gabazine and muscimol leaves basic network stability seemingly unperturbed while clamping the inhibitory circuitry.

As a consequence of $GABA_A$-clamp the phase of virtually all MC_ps shifted to the control TC phase (Φ_{Vm} = 5.74 + [−0.50 0.36] radians, control, versus 2.06 + [−0.59 0.65], $GABA_A$-clamp, p = 0.016, n = 7 cells, circular two sample test, Figures 4F and 4G). The phase of TC_ps on the other hand was completely unaffected (Figures 4H and 4I). Similarly, preferred AP firing phase for MC_ps shifted to the TC phase under $GABA_A$-clamp (Figures S4E and S4F). This strongly suggests that the phase difference between TCs and MCs is set up by inhibitory networks in the OB, that have the effect of shifting the MC phase away from the TC phase.

MCs and TCs Encode Odor Concentrations Differently

This robustness of TC and sensitivity of MC phase in response to network perturbation provokes the question how sensory input might differentially affect the two principal neurons. For high odor concentrations (5%–10% of saturated vapor) MCs and TCs frequently respond to odor stimulation with a significant increase in firing rate (27 of 174 cell-odor pairs are purely excitatory; Figures 5A–5C). As observed under $GABA_A$-clamp, average MC_p phase was again drastically shifted (from 5.01 +[−1.37 0.84] to 1.71 +[−0.68 0.63], p = 0.003, n = 14; Figures 5D and 5E). The average phase of TC_ps, however, remained barely affected (Figures 5F and 5G). Comparing responses at reduced odor concentrations revealed that odor input gradually advanced MC_p phases while consistently leaving average TC_p phases essentially unaltered (Figures 5H, 5I, and S5). This indicates that, as a result of their distinct phase preference, TCs and MCs can encode sensory input differentially; the former in firing rate modulation only and the latter in combined rate change and phase-advance. Furthermore, while neither $GABA_A$-clamp, nor odor presentation affected TC_p phase, MC_p phase was sensitively altered by both manipulations.

Network Models Predict Strong OSN-TC but Weak OSN-MC Excitation, as Well as Strong Feed-Forward Inhibition to MCs

How is such a substantial phase shift between the two principal neuron populations implemented in the OB circuitry? To probe potential mechanisms underlying the measured phase shift we constructed networks of model neurons for a highly simplified OB circuitry (Figure 6A). These consisted of respiration coupled OSN input, MC, and TC as well as three types of interneurons, granule cells (GC), as well as periglomerular cells driven (PGo) and not driven (PGe) by OSN input. Within that simplified connectivity scheme, synaptic weights were drawn randomly. From 6×10^7 such randomly chosen network models we found 1.5×10^4 that reproduced the observed phase difference between MC and TC firing during baseline (black dots in Figure 6B). In a second step we thus assessed the effect of abolishing inhibition in these models. Notably, when analyzing

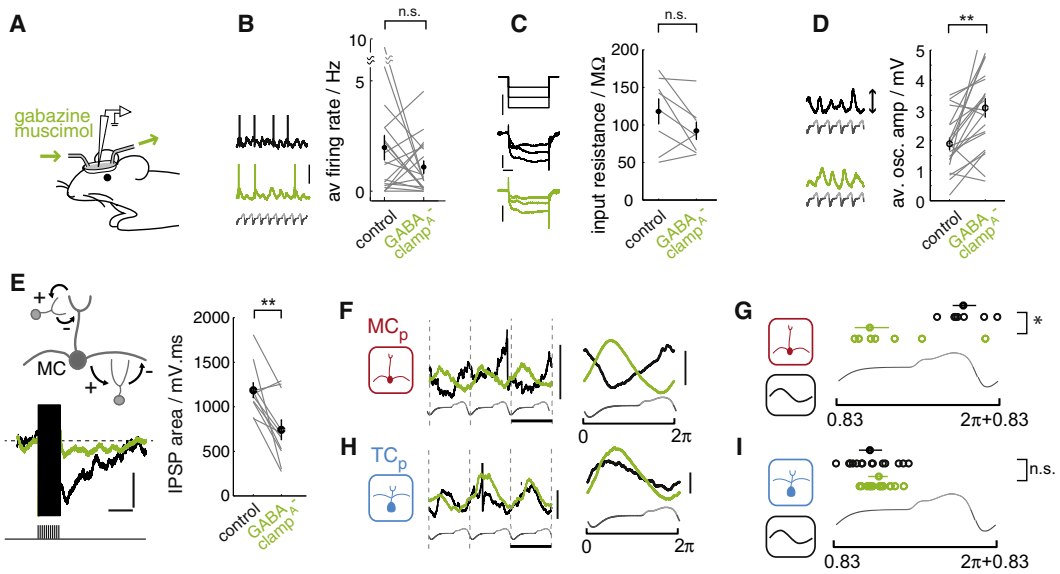

Figure 4. Mitral Cell Phase Is Delayed by Inhibition

(A) Experimental configuration for continuous superfusion of solutions over the exposed brain surface during in vivo whole cell recordings.

(B–D) Quantification of cellular parameters of mitral and tufted cells with combined application of the $GABA_A$ antagonist gabazine and agonist muscimol ("$GABA_A$-clamp"; 0.4 mM and 2 mM, respectively); examples for a single cell are shown on the left (control, black; $GABA_A$-clamp, green): (B) average firing rate (1.97 ± 0.55 Hz control, 1.09 ± 0.28 Hz $GABA_A$-clamp, p = 0.18, n = 19 cells, paired t test), (C) input resistance (118.0 ± 16.6 MΩ control, 92.2 ± 11.5 MΩ $GABA_A$-clamp, p = 0.15, n = 8 cells, paired t test; scale bars represent 0.1 nA, 10mV and 100 ms), (D) subthreshold oscillations (peak-to-peak amplitude 1.89mV ± 0.20mV control, 3.08mV ± 0.31mV, $GABA_A$-clamp; p < 0.005, n = 21 cells).

(E) $GABA_A$-clamp significantly reduces synaptic inhibition in vivo; top left, a scheme of recurrent inhibition; bottom, example from one cell, control, black; $GABA_A$-clamp, green. Scale bars represent 10mV and 250 ms (evoked recurrent IPSPs area 1,186mV ± 82mV × ms control, 741mV ± 109mV × ms, $GABA_A$-clamp, p < 0.005, 11 cells).

(F–I) Comparison of sniff coupling with and without phasic $GABA_A$ inputs. Examples of MC_p and TC_p in control (black) and $GABA_A$-clamp (green; scale bars represent 10mV for raw trace, 2mV for average, sniff cycle length = 332 and 322 ms). APs clipped (F and H). Summary of peak Vm phase during control (black circles) and in $GABA_A$ clamp (green circles), show preferred phase of MC_ps changes (p = 0.008, n = 7 cells; 1/7 morphologically identified, circular two sample test) whereas those of TC_ps do not (p = 0.09, n = 14 cells; 1/14 morphologically identified) (G and I). Values given are mean and 90% confidence intervals (CI). See also Figure S4.

connectivity models that reproduced the collapse of MC phase onto TC phase seen in $GABA_A$-clamp experiments (green dots in Figure 6B), only a distinct region of connectivity space contained high densities of such consistent models (color coding in Figure 6B). These connectivity models were distinguished by a strong PGo →MC and weak PGo →TC inhibition (Figures 6C, 6D, 6G, and 6H). Surprisingly, in addition to the marked differences in inhibitory connection strengths, there was also a distinct difference in the excitatory connections: models consistent with the $GABA_A$-clamp experimental results showed strong OSN →TC and weak OSN →MC connections (Figures 6E–6H). The same connectivity parameters also reproduced the observed phase behavior of TCs and MCs when implemented in a network of compartmental, biophysically realistic neuron models (Figure 6I). Thus, this unbiased, extensive probing of connectivity space suggests a prominent difference in the inhibitory inputs, as well as in the OSN inputs to the two principal neuron classes.

DISCUSSION

Mechanistic understanding of brain function benefits critically from the ability to link physiological properties in vivo and anatomically defined types of neurons. Here we show that the key projection neuron classes in the olfactory bulb, MCs, and TCs, lock their activity to distinct phases of the sniff cycle. This phase shift is established by inhibition in the olfactory bulb that selectively delays mitral cell activity. Consequently, projection neurons respond to excitatory odors differently; TCs readily increase firing rate while MCs additionally show graded phase-advance (Figure 7).

In this study, identifying the key morphological features (Mori et al., 1983) such as the soma and dendritic position was essential in elucidating functional differences clearly. Other means of distinguishing projection neurons in the olfactory bulb such as the depth of recording might be correlated with cell types and thus potentially show similar trends; so far, however, such attempts have failed to distinguish classes of neurons not overlapping in functional measures, such as the sniff locking. One reason for this could be that larger tufted cells such as deep tufted cells (e.g., cells 12 and 13 in Figure S2) are easily confused with MCs if recording depth were the sole measure of identification. More data will be needed to extend this analysis to potential subgroups of TCs, such as superficial, middle, or deep TCs. Our data so far showed no tendency for further distinction in phase locking (Figure 2K). Our method described here to identify

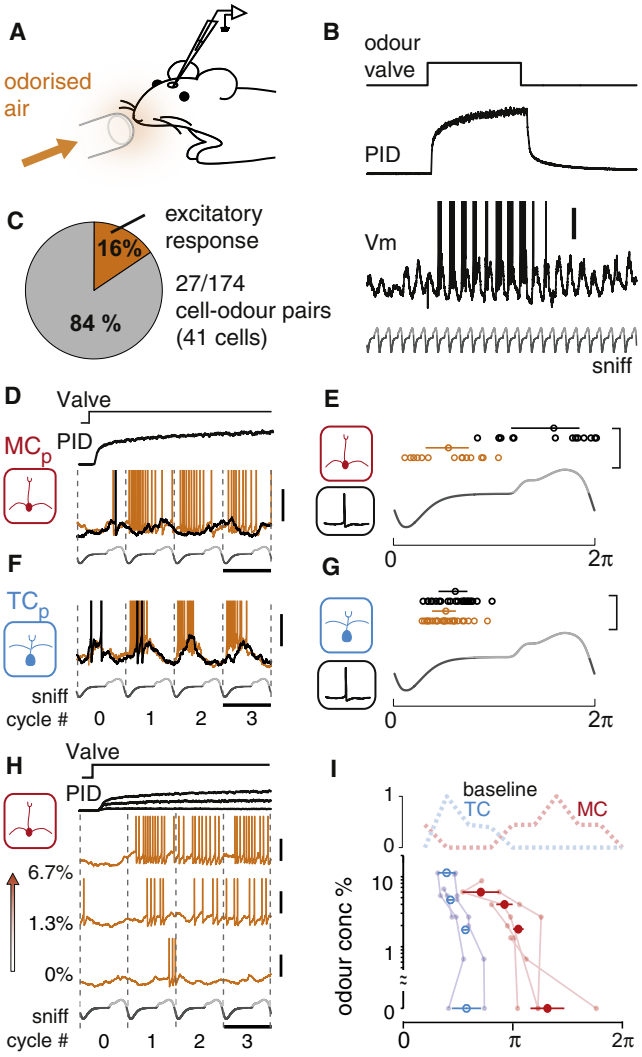

Figure 5. Excitatory Odors Modulate MC Phase but Not TC Phase

(A) Experimental configuration: odors were applied from a flow-dilution olfactometer to an anaesthetized mouse during whole cell recordings.

(B) An example of a photoionization detector signal showing the time course of odor presentation with respect to the valve opening times (top), and corresponding excitatory response evoked in a principal neuron. Scale bar represents 10mV, sniff cycle length = 374 ms.

(C) Immediate excitatory responses are responses with significant increase in firing in the first sniff cycle after the onset of odor presentation and are observed in 16% of all M/T cell-odor pairs recorded.

(D–G) Comparison of sniff-coupling during odor response and baseline. Examples of excitatory odor response (orange) compared to baseline (black): MC_p (D) and TC_p (F). Scale bars represent 10mV. Sniff cycle length = 392 and 414 ms. APs clipped (D and F). Summary of preferred average AP phase during baseline period (black) and during immediate excitatory response (orange) show that preferred average phases of MC_ps advance strongly ([E] $p = 0.003$, $n = 14$ cells; 2/8 morphologically identified) whereas those of TC_ps remain virtually unchanged ([G] $\Psi_{AP} = 1.93 + [-1.20\ 0.85]$ Rad versus $1.63 + [-0.48\ 0.38]$ Rad for baseline and evoked; $p = 0.04$, $n = 26$ cells; paired stats 1/19 morphologically identified) (E and G). Mean and 90% CI for the mean are shown.

(H) An example of phase-advance within one MC_p with increasing odor concentration indicated as % of saturated vapor. Sniff cycle 1 indicates the first complete cycle after the valve opening. Scale bar represents 10mV, sniff cycle length = 380 ms. APs clipped.

(I) Summary of preferred average AP phase for cells where excitatory odors were presented at various concentrations ($n = 3$ cells for TC_p and 4 cells for MC_p). Top: histograms of preferred average AP phases for morphologically identified TCs (blue) and MCs (red) under baseline condition are shown for comparison. Preferred average AP phases for TC_p remain within the TC boundaries for all concentrations, whereas those of MC_p gradually advance with increasing concentration toward the TC phase. Odors used were isoamylacetate, salicylaldehyde, methylsalicylate, eugenol, and annisaldehyde. See also Figure S5.

MCs and TCs based on the sniff locking would help with further investigation of how the two populations may differ, even in cases where morphology is unavailable. Importantly, this is likely to extend to the awake state, where we observed similar strength and diversity of phase preference (Figure S1).

We have investigated the mechanistic basis of the observed phase locking using a newly developed modeling approach that generates a large number of models with randomly chosen connectivity and selects for those that are consistent with the experimental data. The simplicity of the network models has made it possible to sample a vast fraction of connectivity space. This allowed us to extract features of the network that correlate with phase properties consistent with experimental data. While we do not claim that we unequivocally found the actual connectivity implemented in the olfactory bulb, several robust features emerged from this selection procedure. The first observation is the strong feed-forward inhibition, specifically strong PGo-MC connectivity (Figure 6C), which may underlie the GABAergic component crucial in separating MC activation away from the TC activation. Second, the models suggest that MCs are predominantly driven weakly or indirectly and shaped by inhibition. The robustness of the TC phase in turn points toward OSN inputs strongly and directly exciting TCs. A number of recent investigations suggest that the excitatory pathway to MCs from OSNs is rather indirect (Gire and Schoppa, 2009; Najac et al., 2011; Gire et al., 2012). It is exciting to note the consistency of our modeling results with this view. However we cannot exclude an important role of direct transmission from OSNs to MCs, for example by glutamate spillover onto MCs at higher input strengths (Najac et al., 2011). In addition, potential heterogeneities in the intrinsic properties (Angelo and Margrie, 2011; Padmanabhan and Urban, 2010), which we have not addressed in this study, may play a further, amplifying role in differentiating MC and TC physiology.

It has been reported from in vitro investigations that MCs and TCs that belong to a common glomerulus exhibit synchronous activities (Ma and Lowe, 2010). In our hand, a condition similar to this situation may occur during strongly excitatory odor presentations, where MC firing patterns become similar to that of TCs. In other circumstances, it is likely that possible synchrony between MCs and TCs might be overridden by feed-forward inhibition by OSN-PGo-MCs, as well as entrainment of TCs by OSNs rather than mutual excitation.

In explaining the temporal patterns of TC and MC activations observed, on first glance it seems paradoxical that TCs (as well as MCs during strong excitatory odors) are driven during exhalation. However, there is a substantial delay following the inhalation onset to OSN discharge, due to odor molecules

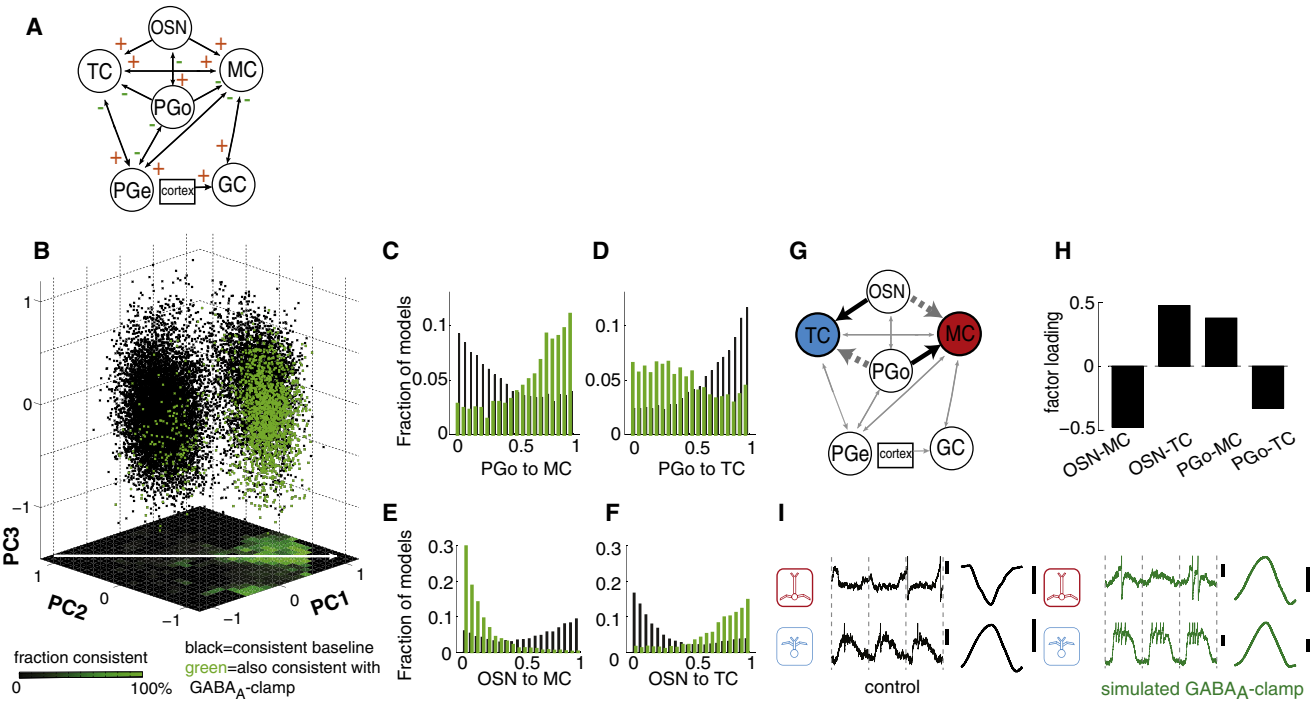

Figure 6. Strong OSN to TC and weak OSN to MC Inputs Reproduce Measured Phase Shift in Models of the Olfactory Bulb

(A) Simplified OB circuitry employed in network models. Arrows indicate the directions of synaptic transmission, while excitatory and inhibitory connections are indicated by the sign. PGo, periglomerular cells driven by OSN input. PGe, periglomerular cells not driven by OSN input.

(B–F) Analyses of 6×10^7 firing rate network models with random connectivity. All models consistent with the phase shift under control conditions were plotted along the first three principal components of a PCA of their connectivity. Of these, models consistent with the experimental result of $GABA_A$-clamp (Figure 4) are plotted in green. The projection onto the PC1-PC2 plane shows the fraction of all phase-shift models that is consistent with the $GABA_A$-clamp. Note the strong asymmetry along the diagonal (white arrow). Histograms of PGo to MC (C) and to TC (D), and of OSN to MC (E) and to TC (F) for all models consistent with the $GABA_A$-clamp result (green, n = 1,826 connectivity's) and the remainder (gray, i.e., models consistent with the MC-TC phase difference but not the $GABA_A$-clamp result, $n = 1.3 \times 10^4$). Models consistent with the $GABA_A$-clamp result show strong PGo-MC, weak PGo-TC, weak OSN-MC, and strong OSN-TC connections.

(G) Connectivity features along the white arrow axis in (B). Thick lines indicate strong factor loading; solid and dashed lines correspond to positive and negative factor loading, respectively.

(H) The four largest components of the direction along which consistent models are separated from not consistent models (white arrow in B).

(I) Connectivity of the firing rate model that is closest to the median of all models consistent with $GABA_A$-clamp (green in B) was implemented in NEURON using standard biophysical PGC and MC models (Cleland and Sethupathy, 2006). Similar to the firing rate models, the biophysically realistic model reproduced experimentally recorded phase difference between MC and TC (control) that converge on the TC phase in simulated $GABA_A$-clamp condition (simulated $GABA_A$-clamp). Right traces are average of 30 sniff cycles. Scale bars represent 5mV (control), 10mV (simulated $GABA_A$-clamp), and 1mV and 4mV (average MC, TC respectively).

binding to olfactory receptors and the relatively slow transduction (Duchamp-Viret et al., 1999). Thus, our results are highly consistent with the notion that the previous inhalation cycle drives depolarization or AP discharge, more than 50–100 ms after the onset of inhalation, in a concentration-dependent manner (Carey et al., 2009). For modest odor concentrations, this implies that MCs lag behind the odor stimulus by approximately half a sniff cycle. Consistent with the rapid responses reported with unit recordings (Cury and Uchida, 2010; Carey and Wachowiak, 2011; Shusterman et al., 2011), TCs in our hands can show an onset in firing rate increase as early as 85 ms after the start of inhalation, while, naturally, the average spiking phase occurs later (Figure S5).

That principal neurons can couple differentially to sniffs has also been noted recently, especially when analyzed over a wide range of sniff frequencies (Carey and Wachowiak, 2011). It is tempting to speculate that the two types of M/TCs reported may indeed correspond to MCs and TCs. In addition, the observed diversity of responses between MCs and TCs may underlie the finding, that principal neurons that belong to a common glomerulus undergo diverse phase changes in response to odors, while showing correlated firing rate changes (Dhawale et al., 2010).

The differential excitatory and inhibitory inputs onto principal neurons would allow olfactory bulb circuits to diversify M/TC activity, instead of simply reflecting OSN inputs, and thus provide olfactory cortex with more processed signals. MCs and TCs are known to differ in axonal projection patterns in the olfactory cortex (Haberly and Price, 1977; Nagayama et al., 2010). Where they overlap anatomically, the mechanism described here will allow distinguishing the two streams of information, by way of temporal characteristics.

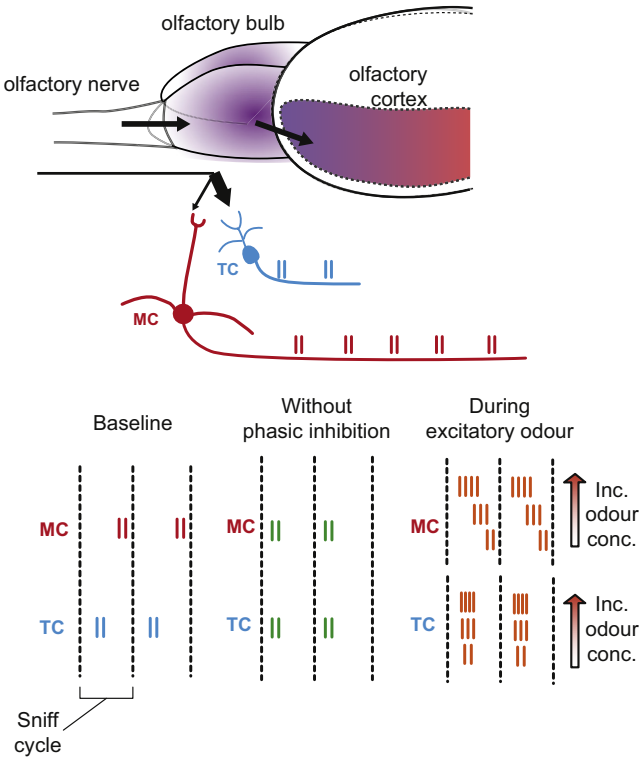

Figure 7. Schematic of the Finding

Principal neurons of the OB, MC, and TC, couple preferentially to opposite phases of the sniff cycle (vertical lines represent action potentials, top and bottom left). This antiphasic coupling at baseline is established by inhibition in the OB, preferentially delaying mitral cell spiking: Blocking phasic inhibition collapses MCs onto the TC phase and leaves TC phase unperturbed (bottom, middle panel). Consequently MCs encode increased excitatory drive (e.g., increased odor concentration) in a graded phase-advance. TCs in contrast respond with a robust firing rate increase at constant average phase (bottom right). Thus, TCs, that project to rostral regions of olfactory cortex and MCs, that innervate both rostral and more caudal regions (top: red, area innervated by MCs; purple, area innervated by TCs as well), not only relay information to spatially overlapping regions of cortex but also operate in distinct temporal windows. This differential phase locking is established by the OB inhibitory circuitry and allows differential encoding of sensory inputs.

A potential implication of our findings is thus that TCs might relay a rapid and crude snapshot of the odor environment, which might be crucial, where speed is of essence. MCs on the other hand transmit delayed but highly processed information to the cortex, which in turn might be central in cases where more complex information needs to be integrated and difficult decisions have to be made. This is consistent with the finding that simple odor identifications and discriminations are performed very rapidly by rodents but it takes longer for more complex odor pairs (Abraham et al., 2004; Rinberg et al., 2006; Uchida and Mainen, 2003) and that inhibition contributes to improved odor discriminability (Abraham et al., 2010). Similar to the visual system, this implies that already at the first stage of processing two spatiotemporally segregated streams of information are established that carry distinct information about the olfactory scenery. Consequently, specific perturbations of the two streams of olfactory bulb output are predicted to have opposing effects on simple odor detection and complex odor discrimination tasks and their different time demands.

Encoding information in specific phases or latencies has been postulated in several systems (Gollisch and Meister, 2008; Mehta et al., 2002; Schaefer and Margrie, 2012). Selective phase preferences of distinct groups of neurons, however, are specifically reminiscent of the picture emerging in the hippocampus where inhibition generates a specific phase code in principal neurons (Mehta et al., 2002; O'Keefe and Recce, 1993). There, the different types of interneurons selectively lock to the underlying oscillatory rhythms in theta, beta, and gamma range (Klausberger et al., 2003). Here we show that principal neurons themselves can lock to distinct phases of an underlying theta cycle establishing two temporally segregated channels for long-range communication as well. It remains to be shown how or under what conditions these temporally segregated yet spatially overlapping pathways will differentially contribute to odor representation in different parts of olfactory cortex.

EXPERIMENTAL PROCEDURES

Electrophysiology

C57BL/6 mice (30- to 50-day-old) were anaesthetized using ketamine (100 mg/kg) and xylazine (20 mg/kg for induction, 10 mg/kg for maintenance) administered intraperitoneally and supplemented as required. All animal experiments were performed according to the guidelines of the German animal welfare law. A subset of experiments was performed in OR174 transgenic mice (Sosulski et al., 2011). A small craniotomy and durectomy were made over the rostrolateral portion of the dorsal olfactory bulb. Whole-cell recordings were made as described previously (Margrie et al., 2002), with borosilicate glass capillaries pulled to 5–10 MΩ resistance when filled with solution containing (in mM): KMeSO4 (130), HEPES (10), KCl (7), ATP-Na (2), ATP-Mg (2), GTP (0.5), EGTA (0.05), biocytin (10), and with pH and osmolarity adjusted to 7.3 and 275–280 mOsm/kg, respectively. Signals were amplified using an Axoclamp 2B amplifier (Molecular Devices, Sunnyvale, CA) and digitized by a Micro 1401 (Cambridge Electronic Design, Cambridge, UK) at 20 kHz. Pharmacological agents were obtained from Tocris Bioscience (Bristol UK) and were dissolved in Ringer solution to the final concentrations of 2 mM and 0.4 mM for muscimol and gabazine, respectively. Ringer solution contained (in mM): NaCl (135), KCl (5.4), HEPES (5), MgCl2 (1), CaCl2 (1.8), and its pH adjusted to 7.2 and 280 mOsm/kg. The drug solution was superfused onto the surface of the OB using a continuous perfusion pump system (Ismatec, IDEX Health & Science, Wertheim-Mondfield, Germany; Figure 4A) during whole cell recordings.

Sniff Measurements

A breathing record was obtained by placing a piezoelectric band (Kent Scientific, Torrington, CT) around the animal's chest. The trough in the chest distension signal during exhalation was used as the start of each breathing cycle (Figure S6) and to trigger odor valve opening. To allow for a direct assessment of inhalation and exhalation, unless stated otherwise, the sniff cycles are indicated as nasal airflow. For calibration, a fast mass flow sensor (FBAM200DU, 1 ms response time; Sensortechnics, Puchheim, Germany) was employed simultaneously with the chest distension signal measurement (Figure S6). Average absolute deviation of estimated inhalation onset from actual inhalation onset for those simultaneous recordings ranged between −0.42 and 0.24 radians (Figure S6).

Odor Presentation

Odors were presented using a custom-made airflow dilution olfactometer with electronic dilution control. Odors (salicylaldehyde, cineol, cinnamaldehyde, methylsalicylate, annisaldehyde, eugenol, and mineral oil) were presented at

0.1%–10% saturated vapor. A photo ionization detector (miniPID, Aurora Scientific, Ontario Canada) was used regularly to determine the time course of odor presentation.

Recordings in Awake Animals

For experiments in head-fixed, awake animals 30- to 50-day-old C57BL/6 mice were implanted with a stainless steel head-plate (6 × 6 × 5 mm), glued with a thin layer of cyanoacrylate covered by dental acrylic (Paladur, Heraeus Holding GmbH, Hanau, Germany) and allowed to recover for 2 days. On the day of the experiments, animals were given meloxicam (2.5 mg/kg) and lidocaine (1%, subcutaneously) preoperatively. Under isoflurane anesthesia (1.75% in air), a craniotomy ~2 mm in diameter was made over the dorsal surface of the olfactory bulb, which was subsequently covered with a thin layer of agarose (5% in the Ringer solution) for stability. A pressure sensor (LBAS500BF6S; Sensortechnics) was attached to the nasal cavity via a metal cannula. Sniff recordings were again calibrated against nasal airflow using a fast mass flow sensor (FBAM200DU, 1 ms response time; Sensortechnics). As sniff waveforms differ in the awake and anesthetized state (Shusterman et al., 2011), we explicitly indicate the estimated start of inhalation in Figure S1. Animals were placed on a custom-built treadmill with their head plate clamped stably in an adjustable holder. The animals were allowed to recover from the isoflurane anesthesia for at least 30 min before recordings commenced. Typical recordings lasted for 4.5 ± 5.1 min. Cells were identified as principal neurons based on depth and input resistance (<200 MOhm).

Histology

For postmortem morphological identification of neurons, mice were perfused following the acute electrophysiological experiment with cold PBS (in mM): NaCl (137), KCl (2.8), KH_2PO_4 (1.5), Na_2HPO_4 (8.1), pH7.4, osmolarity (286 mOsm/kg) followed by 4% formaldehyde solution in PBS. Fixed OBs were cut with a vibratome (Leica, Wetzlar, Germany) and stained with avidin-biotinylated peroxidase (ABC kit, Vector Labs, Burlingame, CA) and the diaminobenzidine reaction. Stained cells, as well as the OB layers (mitral cell layer, MCL; bottom of the glomerular layer, GL), were traced using a Neurolucida system (Micro Bright Field, Williston, VT).

Data Analyses

Electrophysiological data was analyzed with Spike 2 (Cambridge Electronic Design, Cambridge, UK), MATLAB (MathWorks, Natick, MA). Unless noted otherwise, all recordings were aligned to the sniff cycle (Shusterman et al., 2011).

Confidence intervals for circular data were obtained by a Bootstrap method. Briefly, random subsets of data were chosen 100 times from each data set. For each random subset, the deviation of its average phase from the population mean was calculated. These deviations were rank ordered and those at the 5th and 95th ranks were taken as the 90% confidence interval of the mean. Such confidence intervals were used to assess the stability of preferred phase under control conditions (see Figure S7).

Statistical comparisons of two circular data sets were carried out nonparametrically (Fisher, 1995):

$$\Pr = \left(\frac{N^2}{[M(N-M)]}\right)\sum_{i=1}^{2}\frac{m_i^2}{n_i} - \frac{NM}{N-M}.$$

For each data set the value was calculated, where i = experimental conditions 1 and 2, N = number of all data points, n_i = number of data points for each condition, and m_i is the number of neurons whose preferred phase was smaller (i.e., $\phi_{(ij)} - \phi_{\text{(whole data set)}} < 0$) than the population mean, and $M = m_1 + m_2$. Pr values were then compared against the χ^2 distribution (Fisher, 1995) in order to obtain p values.

Firing Rate Model

Firing rate models (6 × 10^7) of the OB network based on key features of the known anatomy (Wachowiak and Shipley, 2006) were constructed from two excitatory principal neurons (one TC and one MC) together with three interneurons (periglomerular cells driven [PGo] and not driven [PGe] by OSN input, as well as a granule cell), with parameters given in Table S1. For each model the overall connectivity architecture was as shown in Figure 6A. The synaptic weight for each connection was chosen randomly from a uniform distribution in the range (0–1). Drawing connectivity parameters from Gaussian distributions with mean 0.5 and SD of 0.2 resulted in essentially identical results as in Figures 6C–6F. Four additional parameters were sampled similarly, namely, respiratory phase and strength of cortical feedback onto GC with respect to OSN respiratory phase and bias currents to set MC and TC excitabilities respectively. OSN activity was modeled by

$$I_{OSN} = \begin{pmatrix} 0.013 \times \sin\left(\frac{0.6\pi t}{750}\right) + 0.005 & 0 < t \le 750 \\ 0.013 \times \cos\left(\frac{0.5\pi(t-750)}{2250}\right) + 0.005 & 750 < t \le 3000 \end{pmatrix}$$

in nA, with t in units of 0.1 ms, giving rise to a cycle length of 300 ms.

The firing rate models were generated on a multicore processor system with the x86-64 instruction set. The Bogacki-Shampine method was used in MATLAB to solve $dR_j = -R + f(R, C, N_j)/t_j$, where R is the firing rate vector, C the connectivity matrix, N_j the single neuron parameters, and t_j the membrane time constant for the j^{th} neuron. The nonlinearity function f was given by: $f(R, C, N_j) = 1/(1 + e^{(slope_j \times (half_j - \sum c_{ij} \times R_j) - I_{extj})})$, whose shape depended on the single cell parameters, t, *slope*, *half*, and I_{ext} give in Table S1.

Model Selection

The models were assessed for consistency with experimental observations during control as well as the $GABA_A$-clamp conditions. For the first round of selection, models were deemed consistent with the phase difference between MCs and TCs if the circular cross correlation (Fisher, 1995) between MC and TC firing rate vectors showed a sufficient global maximum (>0.7) within the 180° ± 35° interval. Of these models, those where MC and TC firing rates were neither zero nor saturated were deemed "consistent with control conditions" (total of 1.5 × 10^4, corresponding to 0.03% of all models). This was assessed using the position of the Jacobian in firing rate space. In the second round of selection, models were deemed "consistent with $GABA_A$-clamp results" if MC phase collapsed onto TC phase ± 40° in simulated $GABA_A$-clamp. This resulted in 1,826 models consistent with $GABA_A$-clamp results. To assess the robustness of each of these models, we varied all connectivity parameters simultaneously by different degrees; the maximum variation ranged from 0% to 30% of total synaptic strength (in steps of 10%), where each variation was drawn from a uniform distribution. Each model was varied 20 times for each jitter range so that a fraction of connectivity still consistent with the $GABA_A$-clamp results could be determined. A sigmoidal fit was used to determine the robustness of each model, defined as the jitter range at which half of the modified connectivity still remained consistent with the experimental results. This robustness varied widely between models (5.02 – 26.68, 9.43 ± 2.78 [mean ± SD] as determined by the sigmoidal fit over the 10%, 20%, 30% jitter values). Nevertheless, the key connectivity features (strong OSN →TC, weak OSN →MC) were maintained.

NEURON Implementation

The connectivity matrix closest to the median of all models consistent with $GABA_A$-clamp was implemented in NEURON (Hines and Carnevale, 1997) using published single cell parameters (Cleland and Sethupathy, 2006). The TC parameters were modified from those of the MC by reducing dendritic membrane area (Figure 2I).

Synaptic connections were implemented as previously described (Cleland and Sethupathy, 2006) with kinetic parameters as listed in Table S2 and the following scaling factors: for synapses, connection strength of 1 in the firing rate model was scaled to 0.3 mS, and bias currents for MC and TC to ±0.2 nA. The cortical feedback onto GC was a time shifted OSN signal. Low pass filtered (cutoff 1 kHz) Gaussian noise with an average of 0mV, and SD varying in the range 0.01–0.2mV depending on the input resistance of neurons, was added to all OB neurons.

Simulating GABA-Clamp

To simulate the $GABA_A$-clamp condition, in the firing rate model inhibitory synaptic weights were set to zero while maintaining MC and TC firing rates

by adjusting the bias current to the principal neurons by an iterative algorithm. Approximately 0.5% of models were discarded due to lack of convergence within 20 iterations. In the NEURON implementation, the $GABA_A$-clamp condition was modeled by setting inhibitory synaptic weights to zero and introducing a decreasing cellular excitability to mimic the effect of muscimol by adding an additional ohmic "chloride" conductance with $E_{rev} = -70mV$ or by increasing the leak driving force. Both approaches yielded the same robust collapse of the MC phase onto the TC phase.

Morphological Clustering

The morphological data collected in Neurolucida was exported into MATLAB using a custom written procedure. From this the following parameters were extracted: distance from soma to mitral cell layer (MCL) and glomerular layer (GL; minimum distance between a point associated with the MCL or GL and a point associated with the soma); mean relative dendritic position in the external plexiform layer (EPL; distance of each dendritic segments to the MCL divided by the sum of the distance to the MCL and GL weighted by volume and averaged over all dendritic segments); soma area (area of the traced soma contour) and total dendritic length. EPL was defined as the region lying between the MCL and GL.

Reconstructed neurons were then classified into two distinct subgroups using an EM algorithm on the parameters listed above, constrained to a minimum of three neurons per cluster. Tuft parameters as well as dendritic diameters were omitted from the cluster analysis as their staining and reconstruction tended to be less reliable.

SUPPLEMENTAL INFORMATION

Supplemental Information includes eight figures and two tables and can be found with this article online at http://dx.doi.org/10.1016/j.neuron.2012.05.017.

ACKNOWLEDGMENTS

We thank Marlies Kaiser, Ellen Stier and Sebastiano Bellanca for technical assistance, Jenny Davie, Matt Angle, Andreas Draguhn, Johann Bollman, Kevin Franks, and Moritz Helmstaedter for comments on the manuscript and Jan Herb, Matthew Phillips and Gordon Shepherd for discussion. This work was supported by the Max-Planck-Society, DFG SPP1392, Bauer Stiftung and the Alexander von Humboldt-foundation. A.T.S. is a member of the ExcellenzCluster CellNetworks. I.F. and A.T.S. designed and conceived all experiments; M.B., I.F. and A.T.S. designed the model and computational analyses; I.F. performed all experiments apart from awake recordings, which were carried out by M.K., and A.S.; I.F. and A.T.S. analyzed the data with help from M.B. and M.K.; M.B. implemented, analyzed and interpreted the model with advice from I.F. and A.T.S.; I.F. and A.T.S. wrote the article with contributions from all authors. The authors declare no competing financial interests.

Accepted: May 1, 2012
Published: July 25, 2012

REFERENCES

Abraham, N.M., Spors, H., Carleton, A., Margrie, T.W., Kuner, T., and Schaefer, A.T. (2004). Maintaining accuracy at the expense of speed: stimulus similarity defines odor discrimination time in mice. Neuron *44*, 865–876.

Abraham, N.M., Egger, V., Shimshek, D.R., Renden, R., Fukunaga, I., Sprengel, R., Seeburg, P.H., Klugmann, M., Margrie, T.W., Schaefer, A.T., and Kuner, T. (2010). Synaptic inhibition in the olfactory bulb accelerates odor discrimination in mice. Neuron *65*, 399–411.

Angelo, K., and Margrie, T.W. (2011). Population diversity and function of hyperpolarization-activated current in olfactory bulb mitral cells. Sci. Rep. *1*, 50.

Bao, S., Chen, L., Kim, J.J., and Thompson, R.F. (2002). Cerebellar cortical inhibition and classical eyeblink conditioning. Proc. Natl. Acad. Sci. USA *99*, 1592–1597.

Bosman, C.A., Womelsdorf, T., Desimone, R., and Fries, P. (2009). A microsaccadic rhythm modulates gamma-band synchronization and behavior. J. Neurosci. *29*, 9471–9480.

Buonviso, N., Amat, C., Litaudon, P., Roux, S., Royet, J.-P., Farget, V., and Sicard, G. (2003). Rhythm sequence through the olfactory bulb layers during the time window of a respiratory cycle. Eur. J. Neurosci. *17*, 1811–1819.

Cang, J., and Isaacson, J.S. (2003). In vivo whole-cell recording of odor-evoked synaptic transmission in the rat olfactory bulb. J. Neurosci. *23*, 4108–4116.

Carey, R.M., and Wachowiak, M. (2011). Effect of sniffing on the temporal structure of mitral/tufted cell output from the olfactory bulb. J. Neurosci. *31*, 10615–10626.

Carey, R.M., Verhagen, J.V., Wesson, D.W., Pírez, N., and Wachowiak, M. (2009). Temporal structure of receptor neuron input to the olfactory bulb imaged in behaving rats. J. Neurophysiol. *101*, 1073–1088.

Cleland, T.A., and Sethupathy, P. (2006). Non-topographical contrast enhancement in the olfactory bulb. BMC Neurosci. *7*, 7.

Cury, K.M., and Uchida, N. (2010). Robust odor coding via inhalation-coupled transient activity in the mammalian olfactory bulb. Neuron *68*, 570–585.

Dhawale, A.K., Hagiwara, A., Bhalla, U.S., Murthy, V.N., and Albeanu, D.F. (2010). Non-redundant odor coding by sister mitral cells revealed by light addressable glomeruli in the mouse. Nat. Neurosci. *13*, 1404–1412.

Diamond, M.E., von Heimendahl, M., Knutsen, P.M., Kleinfeld, D., and Ahissar, E. (2008). 'Where' and 'what' in the whisker sensorimotor system. Nat. Rev. Neurosci. *9*, 601–612.

Duchamp-Viret, P., Chaput, M.A., and Duchamp, A. (1999). Odor response properties of rat olfactory receptor neurons. Science *284*, 2171–2174.

Fisher, N.I. (1995). Statistical Analysis of Circular Data (Cambridge, UK: Cambridge University Press).

Ghosh, S., Larson, S.D., Hefzi, H., Marnoy, Z., Cutforth, T., Dokka, K., and Baldwin, K.K. (2011). Sensory maps in the olfactory cortex defined by long-range viral tracing of single neurons. Nature *472*, 217–220.

Gire, D.H., and Schoppa, N.E. (2009). Control of on/off glomerular signaling by a local GABAergic microcircuit in the olfactory bulb. J. Neurosci. *29*, 13454–13464.

Gire, D.H., Franks, K.M., Zak, J.D., Tanaka, K.F., Whitesell, J.D., Mulligan, A.A., Hen, R., and Schoppa, N.E. (2012). Mitral cells in the olfactory bulb are mainly excited through a multistep signaling path. J. Neurosci. *32*, 2964–2975.

Gollisch, T., and Meister, M. (2008). Rapid neural coding in the retina with relative spike latencies. Science *319*, 1108–1111.

Haberly, L.B., and Price, J.L. (1977). The axonal projection patterns of the mitral and tufted cells of the olfactory bulb in the rat. Brain Res. *129*, 152–157.

Hines, M.L., and Carnevale, N.T. (1997). The NEURON simulation environment. Neural Comput. *9*, 1179–1209.

Igarashi, K.M., Ieki, N., An, M., Yamaguchi, Y., Nagayama, S., Kobayakawa, K., Kobayakawa, R., Tanifuji, M., Sakano, H., Chen, W.R., et al. (2012). Parallel Mitral and Tufted Cell Pathways Route Distinct Odor Information to Different Targets in the Olfactory Cortex. The Journal of Neuroscience *32*, 7970–7985.

Klausberger, T., Magill, P.J., Márton, L.F., Roberts, J.D.B., Cobden, P.M., Buzsáki, G., and Somogyi, P. (2003). Brain-state- and cell-type-specific firing of hippocampal interneurons in vivo. Nature *421*, 844–848.

Ma, J., and Lowe, G. (2010). Correlated firing in tufted cells of mouse olfactory bulb. Neuroscience *169*, 1715–1738.

Macrides, F., and Chorover, S.L. (1972). Olfactory bulb units: activity correlated with inhalation cycles and odor quality. Science *175*, 84–87.

Macrides, F., and Schneider, S.P. (1982). Laminar organization of mitral and tufted cells in the main olfactory bulb of the adult hamster. J. Comp. Neurol. *208*, 419–430.

Margrie, T.W., and Schaefer, A.T. (2003). Theta oscillation coupled spike latencies yield computational vigour in a mammalian sensory system. J. Physiol. *546*, 363–374.

Margrie, T., Brecht, M., and Sakmann, B. (2002). In vivo, low-resistance, whole-cell recordings from neurons in the anaesthetized and awake mammalian brain. Pflugers Arch. *444*, 491–498.

Mehta, M.R., Lee, A.K., and Wilson, M.A. (2002). Role of experience and oscillations in transforming a rate code into a temporal code. Nature *417*, 741–746.

Miyamichi, K., Amat, F., Moussavi, F., Wang, C., Wickersham, I., Wall, N.R., Taniguchi, H., Tasic, B., Huang, Z.J., He, Z., et al. (2011). Cortical representations of olfactory input by trans-synaptic tracing. Nature *472*, 191–196.

Mori, K., Kishi, K., and Ojima, H. (1983). Distribution of dendrites of mitral, displaced mitral, tufted, and granule cells in the rabbit olfactory bulb. J. Comp. Neurol. *219*, 339–355.

Nagayama, S., Takahashi, Y.K., Yoshihara, Y., and Mori, K. (2004). Mitral and tufted cells differ in the decoding manner of odor maps in the rat olfactory bulb. J. Neurophysiol. *91*, 2532–2540.

Nagayama, S., Enerva, A., Fletcher, M.L., Masurkar, A.V., Igarashi, K.M., Mori, K., and Chen, W.R. (2010). Differential axonal projection of mitral and tufted cells in the mouse main olfactory system. Front Neural Circuits *4*, 120.

Najac, M., De Saint Jan, D., Reguero, L., Grandes, P., and Charpak, S. (2011). Monosynaptic and polysynaptic feed-forward inputs to mitral cells from olfactory sensory neurons. J. Neurosci. *31*, 8722–8729.

O'Keefe, J., and Recce, M.L. (1993). Phase relationship between hippocampal place units and the EEG theta rhythm. Hippocampus *3*, 317–330.

Orona, E., Rainer, E.C., and Scott, J.W. (1984). Dendritic and axonal organization of mitral and tufted cells in the rat olfactory bulb. J. Comp. Neurol. *226*, 346–356.

Padmanabhan, K., and Urban, N.N. (2010). Intrinsic biophysical diversity decorrelates neuronal firing while increasing information content. Nat. Neurosci. *13*, 1276–1282.

Phillips, M.E., Sachdev, R.N., Willhite, D.C., and Shepherd, G.M. (2012). Respiration drives network activity and modulates synaptic and circuit processing of lateral inhibition in the olfactory bulb. J. Neurosci. *32*, 85–98.

Rinberg, D., Koulakov, A., and Gelperin, A. (2006). Speed-accuracy tradeoff in olfaction. Neuron *51*, 351–358.

Schaefer, A.T., and Margrie, T.W. (2012). Psychophysical properties of odour processing can be quantitatively described by relative AP latency patterns in mitral and tufted cells. Front. Syst. Neurosci. *6*, 30.

Schroeder, C.E., Wilson, D.A., Radman, T., Scharfman, H., and Lakatos, P. (2010). Dynamics of Active Sensing and perceptual selection. Curr. Opin. Neurobiol. *20*, 172–176.

Smear, M., Shusterman, R., O'Connor, R., Bozza, T., and Rinberg, D. (2011). Perception of sniff phase in mouse olfaction. Nature *479*, 397–400.

Shusterman, R., Smear, M.C., Koulakov, A.A., and Rinberg, D. (2011). Precise olfactory responses tile the sniff cycle. Nat. Neurosci. *14*, 1039–1044.

Sosulski, D.L., Bloom, M.L., Cutforth, T., Axel, R., and Datta, S.R. (2011). Distinct representations of olfactory information in different cortical centres. Nature *472*, 213–216.

Uchida, N., and Mainen, Z.F. (2003). Speed and accuracy of olfactory discrimination in the rat. Nat. Neurosci. *6*, 1224–1229.

Wachowiak, M., and Shipley, M.T. (2006). Coding and synaptic processing of sensory information in the glomerular layer of the olfactory bulb. Semin. Cell Dev. Biol. *17*, 411–423.

Wachowiak, M., Denk, W., and Friedrich, R.W. (2004). Functional organization of sensory input to the olfactory bulb glomerulus analyzed by two-photon calcium imaging. Proc. Natl. Acad. Sci. USA *101*, 9097–9102.

Welker, W.I. (1964). Analysis of sniffing of the albino rat. Behaviour *22*, 223–244.

Note Added in Proof

While this paper was in press, Igarashi et al. (2012) reported intracellular recordings and detailed morphological reconstructions from mitral and tufted cells. Consistent with our findings, they demonstrated shorter onset latency for odor responses in tufted cells compared to mitral cells.